Modelling *Kepler* red giants in eclipsing binaries: calibrating the mixing-length parameter with asteroseismology

Tanda Li,[1,2,3]★ Timothy R. Bedding,[1,2]★ Daniel Huber,[1,2,4,5] Warrick H. Ball,[2,6,7,8] Dennis Stello,[1,2,9] Simon J. Murphy[1,2] and Joss Bland-Hawthorn[1]

[1]*Sydney Institute for Astronomy (SIfA), School of Physics, University of Sydney, NSW 2006, Australia*
[2]*Stellar Astrophysics Centre, Department of Physics and Astronomy, Aarhus University, Ny Munkegade 120, DK-8000 Aarhus C, Denmark*
[3]*Key Laboratory of Solar Activity, National Astronomical Observatories, Chinese Academy of Sciences, Beijing 100012, China*
[4]*Institute for Astronomy, University of Hawai'i, 2680 Woodlawn Drive, Honolulu, HI 96822, USA*
[5]*SETI Institute, 189 Bernardo Avenue, Mountain View, CA 94043, USA*
[6]*Institut für Astrophysik, Georg-August-Universität Göttingen, Friedrich-Hund-Platz 1, D-37077 Göttingen, Germany*
[7]*Max-Planck-Institut für Sonnensystemforschung, Justus-von-Liebig-Weg 3, D-37077 Göttingen, Germany*
[8]*School of Physics and Astronomy, University of Birmingham, Edgbaston, Birmingham B15 2TT, UK*
[9]*School of Physics, University of New South Wales, Sydney, NSW 2052, Australia*

ABSTRACT

Stellar models rely on a number of free parameters. High-quality observations of eclipsing binary stars observed by *Kepler* offer a great opportunity to calibrate model parameters for evolved stars. Our study focuses on six *Kepler* red giants with the goal of calibrating the mixing-length parameter of convection as well as the asteroseismic surface term in models. We introduce a new method to improve the identification of oscillation modes that exploits theoretical frequencies to guide the mode identification ('peak-bagging') stage of the data analysis. Our results indicate that the convective mixing-length parameter (α) is $\approx$14 per cent larger for red giants than for the Sun, in agreement with recent results from modelling the APOGEE stars. We found that the asteroseismic surface term (i.e. the frequency offset between the observed and predicted modes) correlates with stellar parameters ($T_{\rm eff}$, $\log g$) and the mixing-length parameter. This frequency offset generally decreases as giants evolve. The two coefficients a_{-1} and a_3 for the inverse and cubic terms that have been used to describe the surface term correction are found to correlate linearly. The effect of the surface term is also seen in the p–g mixed modes; however, established methods for correcting the effect are not able to properly correct the g-dominated modes in late evolved stars.

Key words: stars: evolution – stars: oscillations.

1 INTRODUCTION

Stellar models describe internal structures and evolutionary states of stars. The basic equations were established decades ago and are able to reproduce the general features of stars. However, current theoretical models are commonly working with a number of free parameters. The atmospheres of stars can be measured by photometry and spectroscopy, while the stellar masses, ages, and internal structures are mostly provided by models. Thus, both observational and theoretical calibrations are required for a proper understanding of stars. Free parameters, however, undermine the reliability of theoretical models and increase the true uncertainties of modelling results. These parameters need calibrations for different types of

stars, but unfortunately, theoretical tests beyond the solar case are sparse, especially for red giants.

Among *Kepler* red giants, a few have been identified as eclipsing binaries (EBs). Combining eclipses with radial velocities from spectra allows masses and radii of both companions of the binary to be determined from dynamical modelling (Frandsen et al. 2013; Gaulme et al. 2016), providing the key constraints for stars. The structures and evolutionary histories of detached companions are similar to that of single stars, and hence they are a good population for testing the model parameters. Red giants have helium cores and burn hydrogen in a surrounding shell. Characteristics of the core decide the temperature of the H-burning shell and hence determine the total luminosity. Tight constraints on the physics of the models for red giants would require measurements of the core (Lagarde et al. 2015). Modelling the red giants 30 with precise measurements of the solar-like oscillations by *Kepler* can provide powerful constraints on stellar properties (Jiang et al. 2011; Pérez Hernández

et al. 2016). The acoustic modes mainly probe the envelope, but the mixed modes caused by the p- and g-mode coupling probe the properties of the core (Bedding et al. 2011; Mosser et al. 2014; Lagarde et al. 2016). Thus, red giants in binary systems with well-defined oscillating patterns offer an important opportunity to test free parameters in stellar models.

Low-mass dwarfs and red giants have convective envelopes, where the energy transport is dominated by convection. Simulating the real dynamic process for the whole region comes with great difficulties in computation; hence, a mixing-length approximation is adopted in stellar evolution models. The basic idea of the mixing-length theory is to define a characteristic length for a fluid parcel, over which it maintains its original properties before mixing with the surrounding fluid. The mixing-length parameter ($\alpha \equiv l/H_p$) characterizes this length in the stellar model, where l is the mixing length and H_p is the pressure scale height. For low-mass red giants, the value of α mainly correlates with the total radius and the structure of the envelope. With the independent measurements of masses and radii, as well as the internal structures probed by asteroseismology, this parameter could be constrained properly by seismic red giants in EBs.

The surface term is the systematic offset of individual frequencies between models and observations and arises from poor modelling of the near-surface layers (Christensen-Dalsgaard, Däppen & Lebreton 1988; Christensen-Dalsgaard et al. 1996; Christensen-Dalsgaard & Thompson 1997). Roxburgh & Vorontsov (2003) suggested using the ratio of small to large separations to fit models to observations. The advantage of this method is avoiding the uncertainty of the outer layers since the ratio is mainly determined by the interior structure. Kjeldsen, Bedding & Christensen-Dalsgaard (2008) fitted oscillation frequencies of the Sun and three well-identified Sun-like dwarfs with the surface term corrected by a power law. The approach showed good agreement and has been widely applied to other stars. A later update of the surface-correction formulas given by Ball & Gizon (2014) took mode inertia into account and modelled the surface effects by terms proportional to ν^{-1}/I and ν^3/I based on the discussion of potential asymptotic forms for frequency shifts by Gough (1990). Sonoi et al. (2015) further applied 3D hydrodynamical simulations to derive expressions for the surface correction. The surface term is strongly correlated to surface properties, such as effective temperature and surface gravity. It also relates to model parameters, especially the mixing-length parameter, that determine the structure of the envelope. For this reason, the surface term calibrated to the Sun does not apply directly to other stars and all current methods introduce free parameters because of the uncertainty of the surface layers. The seismic red giants in EBs, as mentioned above, provide us some of the best constrained stars apart from the Sun and they can be the ideal sample for studying the surface term in evolved stars.

In this work, we selected six *Kepler* red giants in EBs with detectable solar-like oscillations from Gaulme et al. (2016) for calibrating the mixing-length parameter and the surface term. We used 4 yr of *Kepler* data to get seismic frequencies and then generate theoretical models for each star. All available observed constraints, namely mass, radius, atmospheric parameters, and stellar oscillations, are used for the calibrations.

2   *Kepler* EB TARGETS

2.1   Target selection

In this work, we used red giants in detached EBs from Gaulme et al. (2016), who used photometric data from the *Kepler* mission and

spectra obtained by the 3.5 m ARC telescope at APO (ARCES) and the Sloan Digital Sky Survey (APOGEE) for measuring eclipses and radial velocities of the binaries. These binary systems each comprise one dwarf and one giant ranging from 1.0 to 1.6 M$_\odot$. The giants are slightly more massive than their dwarf companions. The companions are sufficiently distant for them to evolve independently, because the separations are roughly 10–20 times the radii of the primary stars. From the sample, we selected six red giants showing high-S/N solar-like oscillations as our targets. Fundamental stellar parameters of the selected stars are summarized in Table 1. Obvious systematic differences can be seen in the effective temperatures and metallicities between ARCES and APOGEE. Because both observations were based on high-resolution spectra, we used their average T_{eff} and [Fe/H] and the mean uncertainties of the two parameters in this work, which were also given in Table 1.

2.2   Stellar oscillation and data analysis

We used *Kepler* long-cadence data and the SYD pipeline (Huber et al. 2009) to extract solar-like oscillations of the six red giants. The reduction steps for preparing light curves include cutting out safe modes, correcting the jumps, removing long-period variation by a high-pass filter and the eclipses using the orbital periods in Gaulme et al. (2016). The top panel in Fig. 1 includes the normalized light curves of KIC 9970396 after the reduction. We then calculated power spectra, estimated the region of power excess, fitted to and corrected for the background on power spectra. The bottom panel in Fig. 1 shows the background-corrected power spectra of KIC 9970396. It should be noted that the unit S/N indicates the ratio between the power density of stellar oscillations and the power density of the background.

Because the long-term variations (from eclipses, instrumental drifts, and stellar spots) and the granulation background had been removed from the power spectra we used to study stellar oscillation, the noise is mainly white. The power spectrum of white noise follows a chi-square distribution with 2 degrees of freedom in the frequency domain (Chaplin et al. 2002). We used the frequency bins from 5 to 290 µHz to calculate the probability density function (PDF) of the power density, which can be seen in the bottom-right panel in Fig. 1. The larger the power excess over the white noise distribution, the more likely that power comes from stellar signal. For the PDF of a given spectrum, a cumulative probability can be set up to separate the signal and the noise. And we used a 95 per cent threshold. To evaluate the probability of each frequency bin being signal statistically, we applied Monte Carlo simulations and produced 1000 simulated power spectra by multiplying the power spectrum by a random noise distribution following χ^2 with 2 degrees of freedom. For each simulated power spectrum, we used the 95 per cent threshold and marked every frequency bin by a flag of 'signal' or 'noise'. Lastly, each frequency bin on a power spectrum had 1000 flags. And the percentage of the 'signal' flags was used to describe its signal probability ($\mathcal{P}_{signal}$ hereafter). In the bottom-left panel in Fig. 1, the colour code shows $\mathcal{P}_{signal}$ of the frequency bins in $\nu_{max} \pm 5\Delta\nu$ of KIC 9970396. After the above analysis, the weight of each frequency bin in the following process could be evaluated by its $\mathcal{P}_{signal}$.

Peak bagging of individual frequencies was then carried out. Low-degree p modes are essentially equidistant in frequency, so for

Table 1. Observations of the six *Kepler* EBs. The first column gives the KIC number; the second to fourth columns include atmospheric parameters; the sixth to eighth columns show the mass, radius, and surface gravity obtained by Gaulme et al. (2016) from dynamical modelling; and the last two columns list the asteroseismic observables ($\Delta\nu$ and ν_{max}) extracted by the SYD pipeline (Huber et al. 2009).

Star	Spectroscopic parameters				Dynamical modelling[a]			Asteroseismology[b]	
	T_{eff} (K)	$\log g$ (dex)	[Fe/H] (dex)	Ref.	M ($M_\odot$)	R ($R_\odot$)	$\log g$ (dex)	$\Delta\nu$ (μHz)	ν_{max} (μHz)
KIC 4663623	4812(92)	2.7(2)	−0.13(06)	ARCES	1.4(1)	9.8(3)	2.60(3)	5.18(1)	53.5(7)
	4803(91)	2.7(1)	0.16(04)	APOGEE					
	4808(92)	–	0.01(05)	Adopted					
KIC 5786154	4747(100)	2.6(2)	−0.06(06)	ARCES	1.06(6)	11.4(2)	2.35(2)	3.51(1)	30.1(4)
	4747(100)	–	−0.06(06)	Adopted					
KIC 7037405	4516(36)	2.5(2)	−0.34(06)	ARCES	1.25(4)	14.1(2)	2.24(1)	2.78(1)	22.2(7)
	4542(91)	2.3(1)	−0.13(06)	APOGEE					
	4529(64)	–	−0.24(06)	Adopted					
KIC 8410637	4699(91)	2.7(1)	0.16(03)	APOGEE	1.56(3)	10.7(1)	2.57(1)	4.63(1)	46.3(9)
	4800(80)	2.8(2)	0.08(13)	Frandsen et al. (2013)					
	4750(86)	–	0.12(08)	Adopted					
KIC 9540226	4692(65)	2.2(2)	−0.33(04)	ARCES	1.33(5)	12.8(1)	2.349(8)	3.19(1)	27.8(4)
	4662(91)	2.5(1)	−0.16(08)	APOGEE					
	4677(78)	–	−0.25(06)	Adopted					
KIC 9970396	4916(68)	3.1(1)	−0.23(03)	ARCES	1.14(3)	8.0(2)	2.69(2)	6.30(1)	63.8(5)
	4789(91)	2.7(1)	−0.18(07)	APOGEE					
	4853(80)	–	−0.20(05)	Adopted					

*Notes.*[a]Gaulme et al. (2016).
[b]This work.
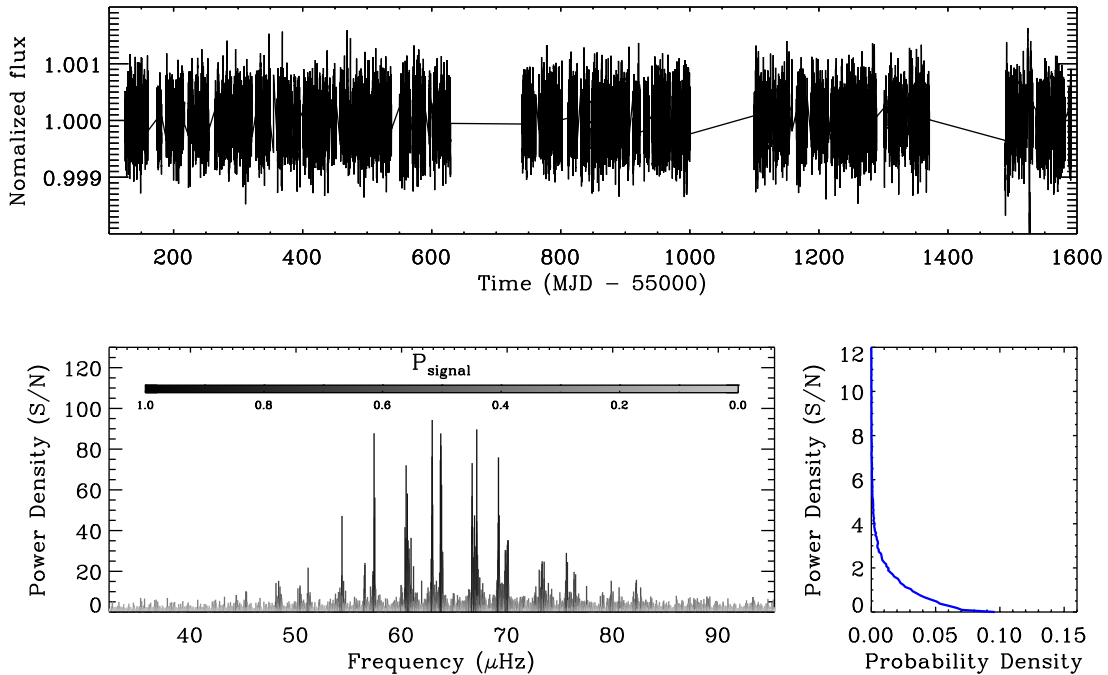
Figure 1. Top: the normalized flux of the *Kepler* light curve of KIC 9970396. Bottom left: background-corrected power spectrum of solar-like oscillations of KIC 9970396 generated by SYD pipeline (Huber et al. 2009). Colour code indicates the probability of each frequency bin being signal ($\mathcal{P}_{\mathrm{signal}}$). Bottom right: the probability distribution of the power density.

a given degree (l) with a separation of $\Delta\nu$, the mode frequency is approximated by

$$\nu_{nl} \approx \Delta\nu \left(n + \frac{l}{2} + \epsilon \right) - \delta_{nl}, \qquad (1)$$

where n is the radial order, ϵ is a parameter related to stellar surface features, and δ_{nl} is the small separation. The large separations for the

stars were calculated by the SYD pipeline. And the small separations are roughly measured by hand in the échelle diagram. We got the first guesses of the modes for $l = 0$ and 2 by this function. The $l = 1$ modes couple to g modes more strongly, and hence multiple modes were seen for a given order (n) in the power spectrum. We measured the median frequency of the multiple $l = 1$ peaks as the initial guess for the most p-like mode. For a proper estimation of
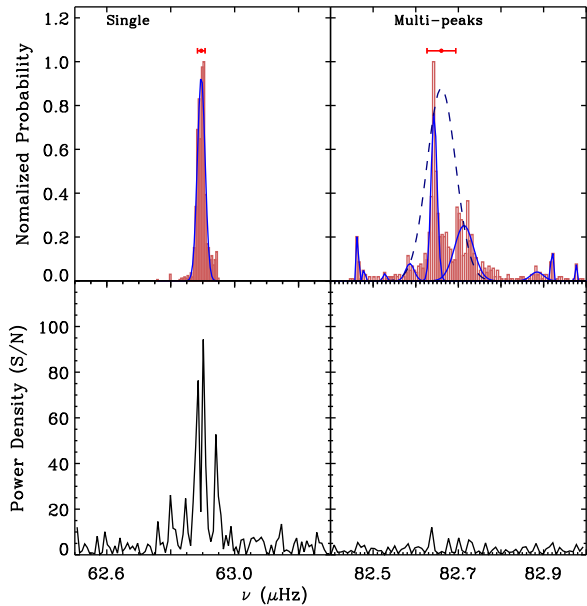
Figure 2. Top: two typical cases of probability distributions of individual $l = 0$ modes based on 1000 Monte Carlo simulations. Left: single peak (high S/N); right: multiple peaks (low S/N). Blue solid lines indicate the Gaussian profile for fitting the distributions. Red error bars in the upper panels are estimates of the mode frequencies and their uncertainties. Bottom: original power spectrum corresponding to the two cases.

individual modes, we applied the same Monte Carlo simulations as mentioned above and generated 1000 simulated power spectra for each star. The least-squares method was then used to fit the individual mode in each simulated power spectrum. A Lorentzian function was used for fitting the modes for $l = 0$ and 2. For fitting the most p-like modes for $l = 1$, we used a Gaussian function to fit the shape of the power excess. The Lorentzian/Gaussian function had three free parameters, namely the centre, the amplitude, and the width. We fixed the baseline as 1.0, which is the median value of the noise in the unit of S/N. The frequency range for fitting $l = 0$ and 2 modes was set as $\pm 0.6\delta\nu_{02}$ centred at the initial guesses. The fitting region for $l = 1$ modes varied for different cases and was determined through visual inspection. We also adopted the $\mathcal{P}_{signal}$ as the weight of every frequency bin when calculating the least-squares of a fitting. First, signal deserves larger weight than noise. Secondly, this fitting method could get reasonable width for the radial modes with low S/N. For some cases when the power excess of a mode shows multiple peaks in the power spectra (e.g. the $l = 0$ mode shown in the bottom-left panel in Fig. 2), the least-squares method without taking into account the weight may fit one of these peaks instead of fitting all of them, giving an unrealistically narrow width for the mode.

After the fitting process above, each mode was measured (the centre of the Lorentzian profile) on the 1000 simulated power spectra. Then a probability distribution of these frequencies could be obtained for estimating a mode. Two typical examples of the probability distribution are given in Fig. 2. For a mode with high S/N (bottom-left panel), a single clear distribution can be obtained (top-left panel). We fitted this probability distribution with a Gaussian profile, and then adopted the centre and 1σ deviation as the estimate of the mode frequency (shown by the red error bar). At low S/N (bottom-right panel), a mode tends to get multiple solutions (top-right panel). For this case, we first fitted each of these solutions individually by a Gaussian (blue solid lines) and then fitted

the centres of these solutions with another Gaussian function (the blue dashed line) for getting the frequency and its uncertainty (the red error bar). The method above was used to determine the radial modes ($l = 0$) and the most p-like modes for $l = 1$ and 2. The identification of individual mixed modes for $l = 1$ will be discussed in Section 4.

3 THEORETICAL MODELS

3.1 Stellar models and input physics

In this work, we used Modules for Experiments in Stellar Astrophysics (MESA, version 8118) to compute stellar evolutionary tracks and generate structural models. MESA is an open-source stellar evolution package that is undergoing active development. Detailed descriptions can be found in Paxton et al. (2011, 2013, 2015).

We adopted the input physics of the calibrated solar model of the 'test_suite' case except for the atomic diffusion. In summary, the solar chemical mixture $[(Z/X)_\odot = 0.0229]$ provided by Grevesse & Sauval (1998) was adopted because solar models calibrated with this mixture (Bi et al. 2011) fit the internal structures from helioseismic inversion better than those with more recent measurements (Asplund, Grevesse & Sauval 2005; Asplund et al. 2009). To determine initial abundances of hydrogen and helium (X_{init} and Y_{init}) for a given content of heavy elements (Z_{init}), we used the following formula:

$$Y_0 = 0.249 \tag{2}$$

$$Y_{init} = Y_0 + \frac{\Delta Y}{\Delta Z} Z_{init} \tag{3}$$

$$X + Y + Z = 1. \tag{4}$$

The primordial helium abundance (Y_0) is determined by Planck Collaboration XIII (2016) using the Planck power spectra, Planck lensing, and some external data such as baryonic acoustic oscillations. The ratio $\Delta Y/\Delta Z$ in equation (3) can be computed by the initial abundances of helium and heavy elements of the Sun. We adopted the $Y_{\odot,init}$ and $Z_{\odot,init}$ of the calibrated solar model given by Paxton et al. (2011), which are 0.2744 and 0.0191 (different from the present-day abundances of 0.243 and 0.0170), and hence the ratio $\Delta Y/\Delta Z$ is 1.33. The MESA ρ–T tables are based on the 2005 update of OPAL EOS tables (Rogers & Nayfonov 2002), and OPAL opacity for the solar composition of Grevesse & Sauval (1998) supplemented by the low-temperature opacity (Ferguson et al. 2005) are used. The mixing-length theory of convection is implemented, and $\alpha \equiv l/H_p$ is the mixing-length parameter for modulating convection. Convective overshooting is set as described by Paxton et al. (2011, Section 5.2) and the overshooting mixing diffusion coefficient was

$$D_{OV} = D_{conv,0} \exp\left(-\frac{2z}{fH_p}\right), \tag{5}$$

where $D_{conv,0}$ is the mixing-length theory-derived diffusion coefficient at a user-defined location near the Schwarzschild boundary, z is the distance in the radiation layer away from the location, and f is a free parameter to change the overshooting scale. The photosphere tables are used as the set of boundary conditions for model atmosphere.

3.2 Stellar oscillation model

The Aarhus adiabatic oscillation package (ADIPLS) is a simple and efficient tool for the computation of adiabatic oscilla-

Table 2. Input parameters and observed constraints for the grid computation.

| KIC | Grid ranges and spacing | | | | Observed constraints | | | |
	$M/\delta M$ (M$_\odot$)	[Fe/H]/δ [Fe/H] (dex)	$\alpha/\delta\alpha$	$f_{ov}/\delta f_{ov}$	T_{eff} (K)	[Fe/H] (dex)	$\log g$ (dex)	R (R$_\odot$)
4663623	1.30–1.40/0.01	−0.19 to +0.21/0.05	1.72–2.52/0.10	0.008–0.020/0.004	4808(100)	0.01(20)	2.57(3)	9.8(3)
5786154	1.00–1.12/0.01	−0.16 to +0.04/0.05	1.72–2.52/0.10	0.008–0.020/0.004	4747(100)	−0.06(06)	2.35(2)	11.4(2)
7037405	1.21–1.29/0.01	−0.44 to −0.04/0.05	1.72–2.52/0.10	0.008–0.020/0.004	4529(110)	−0.24(20)	2.24(1)	14.1(2)
8410637	1.53–1.59/0.01	−0.05 to +0.20/0.05	1.72–2.52/0.10	0.008–0.020/0.004	4750(150)	0.12(17)	2.57(1)	10.7(2)
9540226	1.28–1.38/0.01	−0.38 to −0.08/0.05	1.72–2.52/0.10	0.008–0.020/0.004	4677(110)	−0.25(17)	2.349(8)	12.8(1)
9970396	1.11–1.17/0.01	−0.26 to −0.11/0.05	1.72–2.52/0.10	0.008–0.020/0.004	4853(150)	−0.20(10)	2.69(2)	8.0(2)

tion frequencies and eigenfunctions for general stellar models (Christensen-Dalsgaard 2008, 2011). It was used for computing all theoretical seismic modes in this work. Input parameters for ADIPLS follow the suite for red giants included in the package. It should be noted that structural models generated by MESA (Format FGONG, http://www.astro.up.pt/corot/ntools/docs/Corot_ESTA_Files.pdf) are redistributed for calculating seismic mixed modes. The number of structural shells (N_{Grid}) after redistribution could slightly change the results of frequencies. We tested some fitting models with N_{Grid} from ∼2000 to ∼20 000. And computed frequencies become stable when N_{Grid} is greater than ∼6000. For all the calculations with ADIPLS, we finally redistributed structural models into 9601 shells.

3.3 The surface correction

We used the combined expression and the method described by Ball & Gizon (2014) for correcting the surface term. Based on the discussion of potential asymptotic forms for frequency shifts (Gough 1990), the correction formula is a combination of inverse and cubic terms:

$$\delta\nu = (a_{-1}(\nu/\nu_{ac})^{-1} + a_3(\nu/\nu_{ac})^3)/I, \tag{6}$$

where a_{-1} and a_3 are coefficients adjusted to obtain the best frequency correction($\delta\nu$). The method to determine these two coefficients for a given set of observed and model frequencies was described by Ball & Gizon (2014). According to the frequency offsets found on the Sun and other well-studied solar-like stars (Kjeldsen et al. 2008; Ball & Gizon 2014), $\delta\nu$ increases with frequency. In equation (6), the surface term is also modulated by the normalized mode inertia, I. The description of I can be found in Aerts, Christensen-Dalsgaard & Kurtz (2010, equation 3.140). To avoid confusion, we note that the output result from ADIPLS (ADIPLS notes, equations 4.3a and 4.3b) in the current version is $I/4\pi$. ν_{ac} in equation (6) is the acoustic cut-off frequency, which is derived from the scaling relation (Brown et al. 1991):

$$\frac{\nu_{ac}}{\nu_{ac,\odot}} \approx \frac{g}{g\odot}\left(\frac{T_{eff}}{T_{eff,\odot}}\right)^{-1/2}. \tag{7}$$

Here we take $\nu_{ac,\odot} = 5000$ μHz from Ball & Gizon (2014). Solar references of effective temperature and surface gravity are $\log g_\odot = 4.44$ and $T_{eff,\odot} = 5777$ K (Cox 2000).

4 THEORETICAL COMPUTATIONS AND RESULTS

4.1 Grid computation

The free input parameters for the grid computation include mass (M), initial abundance of heavy elements (Z_{init}) converted from

metallicity ([Fe/H]), initial abundances of hydrogen and helium (X_{init} and Y_{init}) that are computed by equations (2)–(4) for a given Z_{init}, the mixing-length parameter (α), and the overshooting parameter (f_{ov}). We used the masses and their 1σ uncertainties given by Gaulme et al. (2016) as the range of input M. The input range of [Fe/H] was estimated by both individual measurements of ARCES and APOGEE. The lower limit was calculated with the lower observed [Fe/H] minus its 1σ uncertainty, and the upper limit was got from the higher observed [Fe/H] plus its 1σ uncertainty. For instants, the metallicities of KIC 9970396 given by ARCES and APOGEE are -0.23 ± 0.03 and -0.18 ± 0.07, and hence the input range of [Fe/H] for this star is from -0.26 to -0.11. The grids of input M and [Fe/H] were spaced by 0.01 M$_\odot$ and 0.05 dex, respectively. We tested the mixing-length parameter (α) in a wide range around the solar value (Paxton et al. 2011, $\alpha_\odot = 1.92$). The grid of α is from 1.72 to 2.52 with a step of 0.1. The overshooting parameter f_{ov} was either 0.008, 0.012, 0.016, or 0.020, where the upper limit for this parameter (0.020) was estimated by Magic et al. (2010). We used the MESA astero extension's 'grid search' function to generate the grid. In this way, MESA saves structural models that fit observed constraints for further analysis. We used four global observables of each star as the constraints of the 'grid search', namely the average effective temperature and metallicity from spectra, as well as the surface gravity and radius from the binary studies. We set a cut-off value of total χ^2 as 8.0 for selecting MESA models. (For a χ^2 distribution with 4 degrees of freedom, the probability for χ^2 smaller than 8 is 0.91.) A summary of the grid computation with MESA can be found in Table 2. ADIPLS was then implemented for calculating radial ($l = 0$) and non-radial oscillation modes ($l = 1$ and 2).

4.2 Reordering of theoretical mixed modes

Before discussing the subsequent fitting progress, we address one problem that arises with the current way of applying the surface correction in evolved stars: theoretical mixed modes could lose their original order after their surface terms are corrected. We took the model of KIC 7037405 as an example. Fig. 3 shows the mixed modes for $l = 1$ and 2 in a single order of this model. Theoretical mode inertia are plotted against frequencies before and after the surface correction. Due to the quick change of inertia, p-dominated modes (with the lower inertia) get much larger corrections than their g-dominated neighbours. And the modes obtain a new order after the correction. Similar reordering appears in theoretical $l = 1$ mixed modes of KIC 5786154, KIC 7037405, and KIC 9940226 and in the $l = 2$ modes of all six targets. The reordering happens because the surface corrections for the mixed modes differ by more than the separation between consecutive modes. The g-like modes are less changed by the surface properties than p-like modes due to their large mode inertia. And hence we do not expect a strong
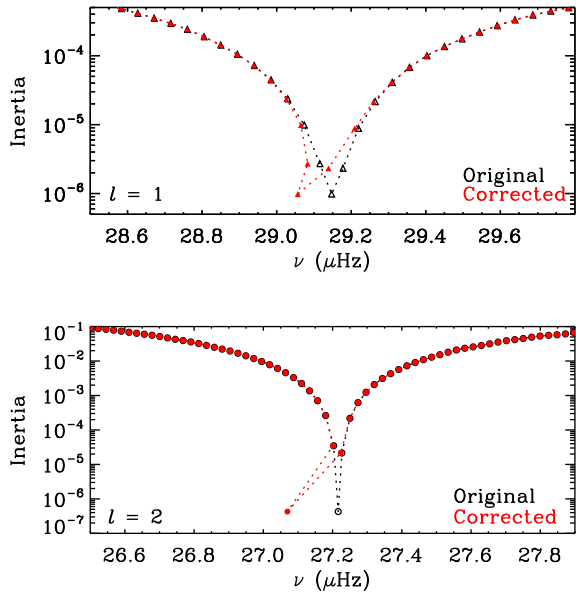
Figure 3. Reordering of mixed modes after surface correction. The upper panel includes the mixed modes for $l = 1$ of the best-fitting model of KIC 7037405, where black open and red filled triangles indicate model frequencies before and after the surface correction. The bottom panel is the same as the upper one but for $l = 2$. The surface-correction coefficients for the model are $a_{-1} = 391.6 \times 10^{-9}$ μHz and $a_3 = -28.9 \times 10^{-7}$ μHz.

surface term for them. However, one thing worth noting is that theoretical mixed modes are solved as the coupling results of p and g modes. If the surface term of the p mode is not being corrected before calculating the coupling, the mixed modes will also be affected.

A proper way to test this issue could be correcting the acoustic wave before calculating the mixed modes. However, no option is available in the seismic code to do this job. Instead, we changed the structure in the near-surface layers of the input model of ADIPLS. This only alters the acoustic wave, but not the gravity modes because they travel inside the core. Modifying the adiabatic exponent ($\Gamma_1 = (\mathrm{d}\ln p/\mathrm{d}\ln\rho)_{\mathrm{ad}}$) in the near-surface layers is a simple way to modulate the acoustic resonance. However, it should be noted that the structural model after this modification is no longer self-consistent. For the case of the Sun, the surface term starts from 1 Mm below its surface where $T = T_{\mathrm{eff}}$. The depth of this region is roughly 0.15 per cent of the total solar radius. Hence, we only changed Γ_1 in layers that are 0.15 per cent of the total radius below the surface. As shown in the top graph of Fig. 4, we gradually increased Γ_1 in the region from 0.9985 R to the surface. The fractional increase at a given depth followed a Gaussian function (blue dotted line). The centre of the Gaussian profile is right on the top layer. And its amplitude and width are 0.3 and 0.0005R, respectively. The mixed modes for $l = 1$ and 2 calculated with the models before and after modifying the surface-corrected Γ_1 are also given in the middle and bottom panels. It can be found that the change in surface layers affects the most p-like modes. Shifted p modes then change the frequency ranges where p–g coupling happens. Thus, the surface term also affects the mixed modes in an indirect way.

Modifying the stellar structure seems to be a way to repair the indirect effects of the surface term on mixed modes. However, it comes with difficulties in rebuilding the equilibrium of the model. We hence still adopted the correcting formula (equation 6) to correct
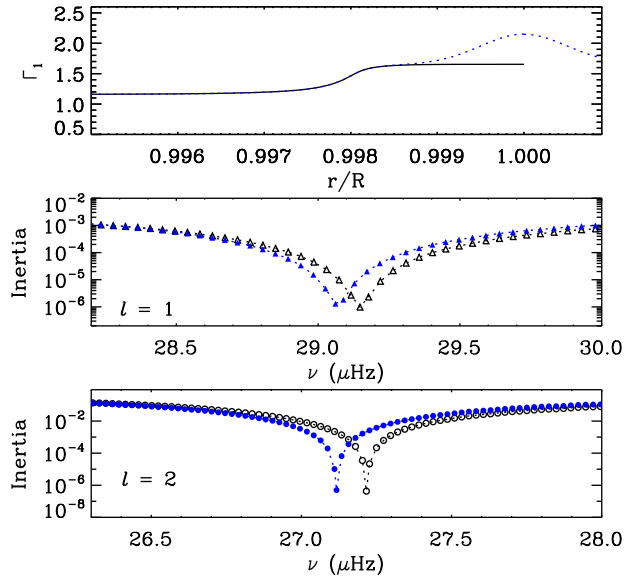

Figure 4. The change of frequency ranges where the p–g coupling happens before and after modifying the structures of the near-surface layers. Top: the distribution of Γ_1 at the near-surface layers before (black solid) and after (blue dots) the modification. The fractional increase of Γ_1 with the depth (r/R) follows a Gaussian function. The centre, width, and amplitude of this Gaussian profile are 1.0R, 0.0005R, and 0.3, respectively. Middle: mixed modes for $l = 1$ of the models before (black open triangles) and after (blue filled triangles) the modification. Bottom: mixed modes for $l = 2$ before (black open circles) and after (blue filled circles) the modification.

model frequencies. To avoid the influence when using it in the following fitting procedures, we checked the model frequencies for all six stars. Hence, only the most p-like modes are considered for these cases. The $l = 1$ mixed modes of the other three stars (KIC 4663623, KIC 8410637, and KIC 9970396) have large enough period spacing to overcome the surface effect without mode order swapping and were used for the following studies. Based on the models of six red giants, ν_{max} greater than $\sim$40 μHz tends to be a safe cut for stars whose mixed modes for $l = 1$ can be adopted. We will mention the identification of observed individual mixed modes for these stars below.

4.3 Identification of individual mixed modes

Peak bagging of individual mixed modes for red giants is complicated by rotational splitting, granulation background, and random noise. On the other side, the theoretical models provide precise oscillation frequencies of mixed modes for every degree and order, which can be a guide to peak bagging.

We first found theoretical models that fit the observed modes for $l = 0$ and 2 (the model with the highest 10 per cent likelihood). These models then guided us to identify $l = 1$ modes. One example, as given in Fig. 5, illustrates the peak-bagging process of mixed modes for KIC 9970396. The model was first constrained by the modes for $l = 0$ and 2 given in the middle panels, as well as a few high-amplitude mixed modes for $l = 1$ (filled symbols), such as the three peaks from 66.7 to 67.2 μHz. All model frequencies were then plotted on the power spectrum (open triangles), suggesting more potential modes like the one at 66.4 μHz, and two at 67.4 and 67.7 μHz. It should be noted that the power of these modes is still significant compared with the background noise level. The method we use for getting the frequencies and uncertainties of
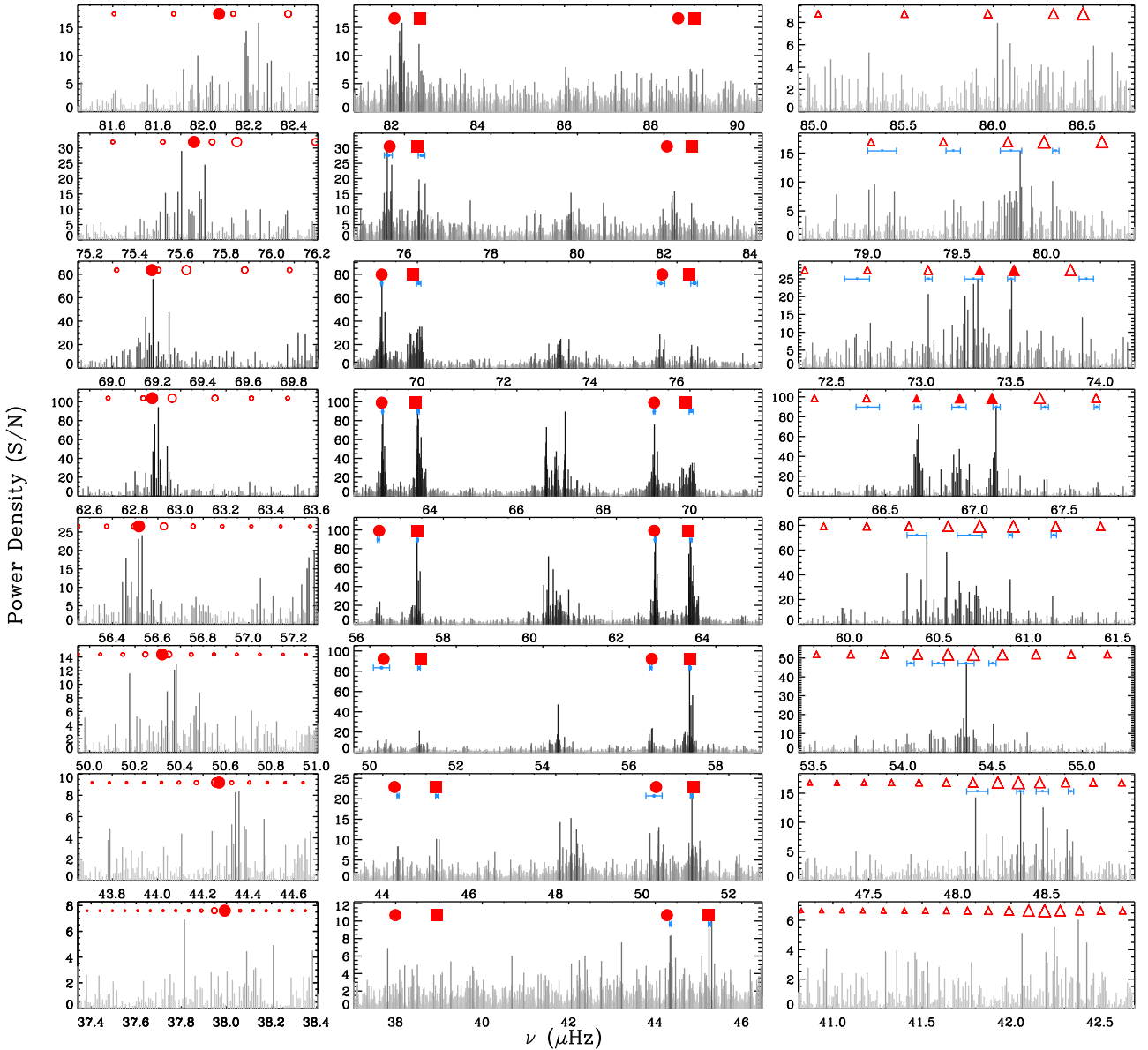
Figure 5. The peak-bagging process of individual mixed modes for KIC 9970396. The whole power spectrum is separated into eight radial-mode orders as shown in the middle. Close inspections of $l = 2$ and 1 modes are plotted on the left and right sides. The colour code was set as the same as that in Fig. 1, indicating the $\mathcal{P}_{\mathrm{signal}}$ of each frequency bin. Red symbols plotted on the top are theoretical frequencies of the best-fitting model. Squares, circles, and triangles in the middle represent the p and most p-like modes for $l = 0$, 1, and 2. Filled symbols are the modes for picking the fitting models, and open symbols are those for guiding the identification of other mixed modes. Circles and triangles on the left and right indicate all theoretical mixed modes in each frequency bin. And their symbol size is scaled with $1/I^2$ (I is mode inertia) by reference to that of the most p-like mode in each degree and order. Larger size indicates the mode to be more p-like and less in inertia. Small blue symbols represent identified observed frequencies.

individual mixed modes is as follows. For a potential mode based on the visual inspection, we flagged the observed peaks with $\mathcal{P}_{\mathrm{signal}} > 0.5$ around the theoretical predictions. The median value of these peaks was adopted as the frequency of this mode. And the difference between the median value and the highest/lowest frequency was measured as the uncertainty. The blue error bars in Fig. 1 represent all of the identified modes and their uncertainties. We also tried to identify the g-dominated modes for $l = 2$ (on the left side). However, no significant mode has been found because of their large inertia. All the identified modes of KIC 9970396 are listed in Table 3. The power spectra and tables of all six stars can be found in Appendix A.

4.4 Calibrating the model parameters

We used a Bayesian method to estimate the mixing-length parameter (α) and the two coefficients for surface correction (a_{-1} and a_3). The agreement between models and observations was first examined by a likelihood function. The observed data for these stars can be divided into three parts. The mass, radius, and atmospheres provide global features; p and the most p-like modes mainly relate to the structure of the envelope; and p–g mixed modes probe the characteristics of the core. Thus, the likelihood ($\mathcal{L}$) for every model comprises these three parts, namely $\mathcal{L}_{\mathrm{glob}}$, $\mathcal{L}_{\mathrm{env}}$, and $\mathcal{L}_{\mathrm{core}}$.

The likelihood of global features was calculated using the masses, radii, and surface gravities from dynamical modelling, as well as

Table 3. Identified oscillation frequencies for star KIC 9970396.

l	ν (μHz)	σ (μHz)
2	44.351	0.021
0	45.255	0.032
2	50.270	0.187
0	51.138	0.029
2	56.496	0.023
0	57.396	0.015
2	62.895	0.012
0	63.717	0.023
2	69.173	0.017
0	70.031	0.050
2	75.626	0.091
0	76.395	0.077
1	48.110	0.060
1	48.350	0.020
1	48.475	0.034
1	48.635	0.016
1	54.040	0.018
1	54.195	0.034
1	54.350	0.016
1	54.498	0.020
1	54.703	0.029
1	60.420	0.110
1	60.650	0.052
1	60.899	0.012
1	61.140	0.015
1	66.400	0.065
1	66.680	0.020
1	66.910	0.040
1	67.120	0.020
1	67.390	0.023
1	67.680	0.015
1	72.640	0.070
1	73.040	0.022
1	73.290	0.051
1	73.501	0.019
1	73.921	0.041
1	79.100	0.100
1	79.477	0.040
1	79.850	0.050
1	80.032	0.032

effective temperatures ($T_{\rm eff}$) and metallicities ([Fe/H]) from spectra. It is described as

$$\mathcal{L}_{\rm glob} = \exp\left(-\frac{1}{2n}\sum_{i=1}^{n}\frac{(x_i - u_i)^2}{\sigma_i^2}\right), \quad (8)$$

where x_i and u_i indicate theoretical and observed parameters, and σ_i is the uncertainties of observations. The likelihood for the envelope was estimated by comparing p and the most p-like mixed modes from models and observations:

$$\mathcal{L}_{\rm env} = \exp\left(-\frac{1}{2n}\sum_{i=1}^{n}\frac{(\nu_{{\rm model},i} - \nu_{{\rm obs},i})^2}{\sigma_{{\rm obs},i}^2}\right). \quad (9)$$

Individual g-dominated mixed modes were identified for KIC 4663623, KIC 8410637, and KIC 9970396 (the other three have the problem with the surface correction), and we used them to estimate the likelihood for the core by

$$\mathcal{L}_{\rm core} = \exp\left(-\frac{1}{2n}\sum_{i=1}^{n}\frac{(\nu_{{\rm model},i} - \nu_{{\rm obs},i})^2}{\sigma_{{\rm obs},i}^2}\right). \quad (10)$$
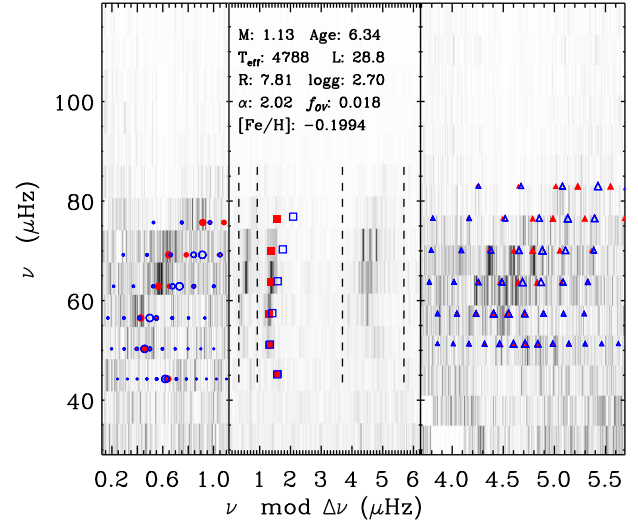
Figure 6. Observed and theoretical échelle diagram of KIC 9970396. Grey-scale is the observed power density. Blue and red symbols indicate model frequencies before and after surface correction. The middle panel includes the whole échelle diagram, where red squares are radial modes. Left- and right-hand panels zoom in on $l = 2$ and 1 modes. Theoretical mixed modes are plotted in different sizes scaled by $1/I^2$ (I is the normalized mode inertia) by reference to the most p-like mode at the same degree and order. The largest symbol indicates the most p-like mode for $l = 1$ and 2 in each order.

These three parts gave the final likelihood, described as

$$\mathcal{L} = \mathcal{L}_{\rm glob}\mathcal{L}_{\rm env}\mathcal{L}_{\rm core}. \quad (11)$$

The best-fitting model of KIC 9970396 based on the likelihood test is given in Fig. 6. It shows that model frequencies fit quite well after the surface correction.

The theoretical models in this work have four independent input parameters, namely mass (M), heavy-element abundance (Z), the mixing-length parameter (α), and overshooting parameter ($f_{\rm ov}$). Along with age (τ) and two coefficients (a_{-1} and a_3), these seven variables specify a particular model. Thus, we can write the probability of a model as

$$p({\rm Model}|{\rm Data}) = p({\rm Model})p({\rm Data}|{\rm Model}) = {\rm prior} \cdot \mathcal{L}, \quad (12)$$

where Model = $\{M, Z, \tau, \alpha, f_{\rm ov}, a_{-1}, a_3\}$ and Data = $\{T_{\rm eff},$ $\log g, [{\rm Fe/H}], R, \nu_{l,n}\}$. $\mathcal{L}$ is the likelihood obtained above. We assumed a flat prior for all model quantities. Then the probability of α, a_{-1}, and a_3 for a star can be calculated by marginalizing over all the other model quantities:

$$p(\alpha) = \int p(M, Z, \tau, \alpha, f_{\rm ov}, a_{-1}, a_3){\rm d}M{\rm d}Z{\rm d}\tau{\rm d}f_{\rm ov}{\rm d}a_{-1}{\rm d}a_3, \quad (13)$$

$$p(a_{-1}) = \int p(M, Z, \tau, \alpha, f_{\rm ov}, a_{-1}, a_3){\rm d}M{\rm d}Z{\rm d}\tau{\rm d}\alpha{\rm d}f_{\rm ov}{\rm d}a_3, \quad (14)$$

and

$$p(a_3) = \int p(M, Z, \tau, \alpha, f_{\rm ov}, a_{-1}, a_3){\rm d}M{\rm d}Z{\rm d}\tau{\rm d}\alpha{\rm d}f_{\rm ov}{\rm d}a_{-1}. \quad (15)$$

Fig. 7 gives the probability distributions of α, a_{-1}, and a_3 for the six stars. The histograms mainly follow Gaussian distributions. Some profiles have a sudden drop rather than a smooth decrease at the boundary. The reason is that the MESA astero 'grid search' function was set to only save models that were in reasonable agreement with the observations ($\chi^2 < 8$). We used a Gaussian function
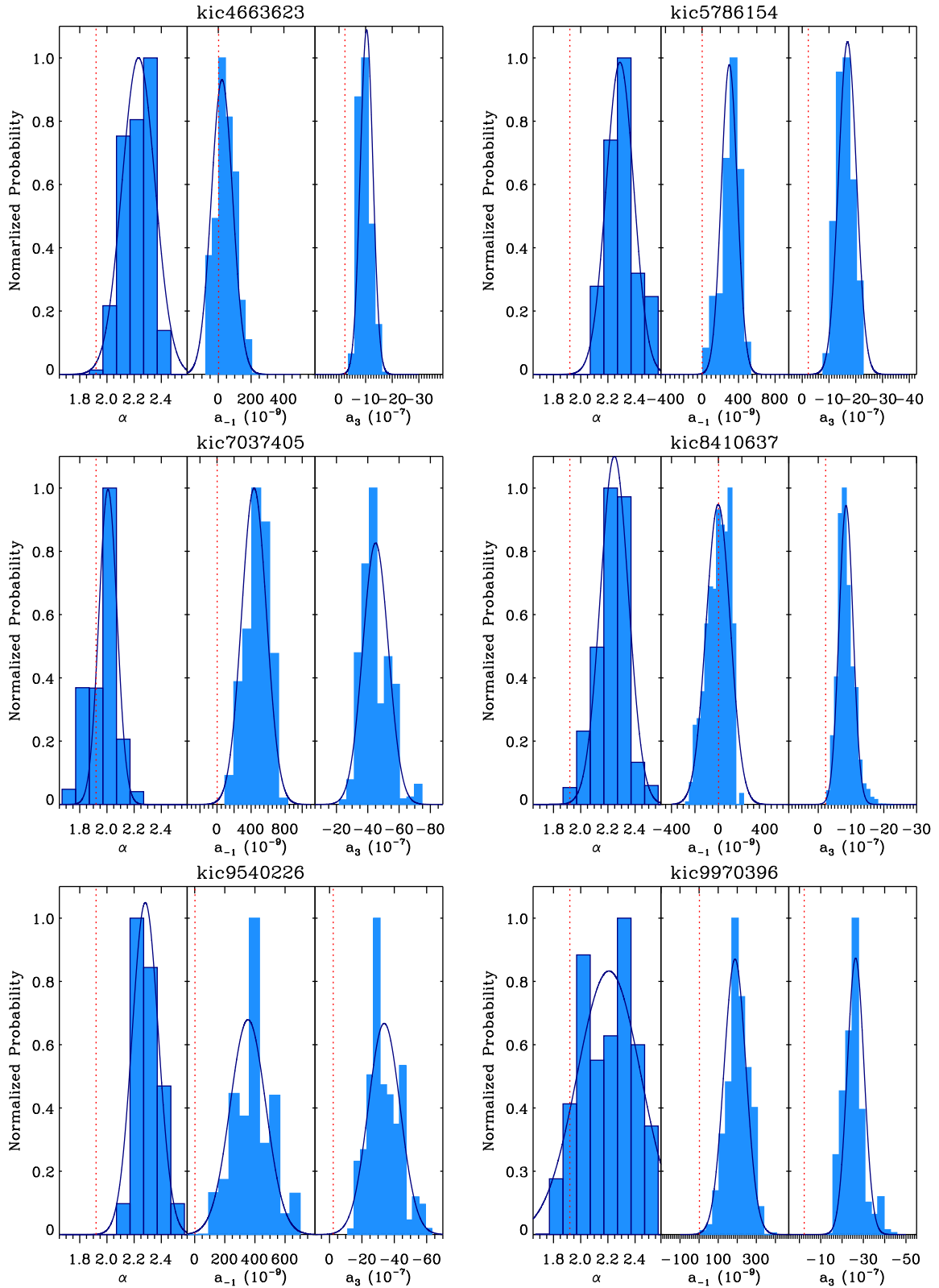
Figure 7. Probability distributions for the mixing-length parameter (α) and the two coefficients (a_{-1} and a_3) for the surface correction. Histograms are normalized proportional to the highest peak. a_{-1} and a_3 are scaled by 10^{-9} and 10^{-7} μHz. Solid curves are the Gaussian profiles for fitting the probability distributions. Red dotted lines indicate solar values, which are 1.92 for α (Paxton et al. 2011), 1.73×10^{-9} μHz for a_{-1}, and -2.25×10^{-7} μHz for a_3 (Ball & Gizon 2014).

Table 4. Calibrated mixing-length parameter and the two coefficients in the surface-correction expression (equation 6).

Star	α	a_{-1} $(10^{-9}\,\mu Hz)$	a_3 $(10^{-7}\,\mu Hz)$
Sun	1.92	1.73	−2.25
KIC 4663623	2.23 ± 0.12	22.50 ± 64.74	-10.4 ± 2.4
KIC 5786154	2.29 ± 0.10	298.9 ± 87.0	-16.9 ± 3.3
KIC 7037405	2.01 ± 0.07	435.0 ± 145.1	-45.0 ± 8.1
KIC 8410637	2.25 ± 0.10	-1.6 ± 102.7	-8.5 ± 2.1
KIC 9540226	2.28 ± 0.10	354.0 ± 117.7	-33.8 ± 9.8
KIC 9970396	2.21 ± 0.23	188.3 ± 57.5	-26.4 ± 3.9

to fit probability distributions, and adopted the centre and 1σ deviation of the Gaussian profile as the central value and the uncertainty. The results are summarized in Table 4.

5 MODEL PARAMETERS

5.1 The mixing-length parameter

The calibrated mixing-length parameters of the six red giants (Table 4) suggest larger α for evolved stars than that for the Sun ($\alpha_\odot = 1.92$). The average mixing-length parameter is about 2.20. However, KIC 7037405 converges at significantly different values (2.00). As mentioned, the determination of α depends greatly on the measurements of the mass (from the binary orbits). Modelling a star with increased mass tends to lead to a smaller mixing-length parameter when other constraints are kept fixed. Hence, systematic errors in mass can bias the results. KIC 7037405, 9540226, and 9970396 were also recently studied by Brogaard et al. (2017). They obtained masses that differ by -2σ for KIC 7037405, 0.96σ for KIC 9540226, and 1.25σ for KIC 9970396. The results suggest that KIC 7037405 could have a larger mixing-length parameter than what was obtained (2.00) while KIC 9540226 and KIC 9970396 may converge at a slightly smaller α.

The average α obtained for our six giants is $\sim 1.14 \pm 0.07$ times the calibrated solar value. This result is similar to that achieved by Tayar et al. (2017) with the APOGEE-*Kepler* targets. Their grid models for the red giants within the range of metallicity ([Fe/H]) from -0.5 to $+0.4$ required a ~ 8 per cent larger α than the Sun to fit the observations. Tayar et al. (2017) also suggested a linear correlation between α and [Fe/H]. However, we did not obtain a clear dependence between the two parameters in our stars.

The realistic simulation of convection is another approach to estimate the mixing-length parameter. Magic, Weiss & Asplund (2015) calibrated α with the STAGGER grid, which predicted slightly smaller values (0.90–0.95 $\alpha_\odot$) for red giants ($T_{\rm eff} \simeq 5000\,K$ and $\log g \simeq 2.5$) than that for the Sun. An earlier work by Trampedach & Stein (2011) found the mixing-length parameter to be 0.96–1.00 $\alpha_\odot$ for the red giants having similar stellar parameters to our stars ($M = 0.8$–2.5 $M_\odot$, $T_{\rm eff} = 4200$–5500 K, $\log g = 2.4$–3.0) through 3D simulations (Trampedach et al. 2014). The ~ 16 per cent difference of the 1D stellar model from the simulations may indicate an improper modelling for the near-surface layers in the 1D model with the current input physics. First, the mixing-length parameter of a star varies for different evolutionary stages (Trampedach et al. 2014; Magic et al. 2015); however, we fixed the mixing-length parameter through the stellar evolution. Secondly, the boundary conditions for red giants can be different from the Sun due to the changes in structures. Moreover, the systematic offsets in observed effective temperatures and metallicities could also affect the results.

5.2 The surface term in evolved stars

The surface effect, which correlates with the near-surface properties, is believed to be a function of $T_{\rm eff}$ and $\log g$ (Sonoi et al. 2015). The comparison between hydrodynamical simulations and stellar models (Ball et al. 2016) suggested an increasing surface term for dwarfs from the spectral type of K5 to F3. Trampedach et al. (2017) estimated the frequency shifts in various types of stars with a grid of convection simulations and also gave a clear correlation between the surface term and atmospheric parameters.

The frequency offsets caused by the surface term in the best-fitting models of our six red giants are given in Fig. 8. All these stars resulted in the offsets of the order of 0.1 µHz at $\nu_{\rm max}$. We compare our results with previous studies in Fig. 9, which gives the distribution of absolute ($\delta\nu$) and relative ($\delta\nu/\nu_{\rm max}$) frequency offsets as a function of the location in the HR diagram. In order to compare with previous results, we also included the six low-luminosity red giants studied by Ball & Gizon (2017) as well as the simulation values given by Sonoi et al. (2015) and Trampedach et al. (2017). Modelling results between low- and high-luminosity red giants show an apparent reduction in both absolute and relative offsets when stars become more evolved. The decreasing $\delta\nu$ on the red giant branch from modelling agrees with the trend predicted by simulation. However, the fractional change ($\delta\nu/\nu_{\rm max}$) does not follow the simulation results.

Apart from the improper modelling for the surface layers, the uncertainty of the mixing-length parameter also affects the surface term. Fig. 10 shows the correlation between the mixing-length parameter and the surface-correction coefficient of the cubic term (a_3). The surface term, as expected, shows a strong dependence on the input α of the model. It varies by a factor ranging from 1.5 to 2 for different stars when the mixing-length parameter changes from 1.9 (the solar value) to 2.2 (the red giants' value). This is to say, if α cannot be handled well, the surface term will come with significant scatter. Hence, the calibrated mixing-length parameters for the six red giants also provide a good constraint on the surface term coefficients. We state here that the degeneracy between α and a_3 does not influence our results in Fig. 7, as we have marginalized over all other variables when deriving the posteriors, so these degeneracies are captured in the uncertainties.

A further comparison of the coefficients of stars at different evolutionary stages is given in Fig. 11. Besides the low-luminosity giants from Ball & Gizon (2017) and the high-luminosity giants in this work, we also selected 27 main-sequence dwarfs from the LEGACY sample. These stars cover a range from 0.75 to 1.15 $M_\odot$, $T_{\rm eff} = 5500$–6200 K, and $\log g = 4.2$ –4.5. The comparison shows a significant increase of a_{-1} and a_3 with stellar evolution. We note that the increase is because of the growth of mode inertia, not indicating an increasing surface term with stellar evolution. In contrast, the fractional frequency offsets ($\delta\nu/\nu_{\rm max}$) decrease with stellar evolution. Moreover, a good linear relation between a_{-1} and a_3 shows in our six red giants: $a_3 \sim -10\,a_{-1}$. This agrees with the simulation result from Trampedach et al. (2017), who found a stable ratio between the inverse and cubic terms for red giants with similar $T_{\rm eff}$ and $\log g$.
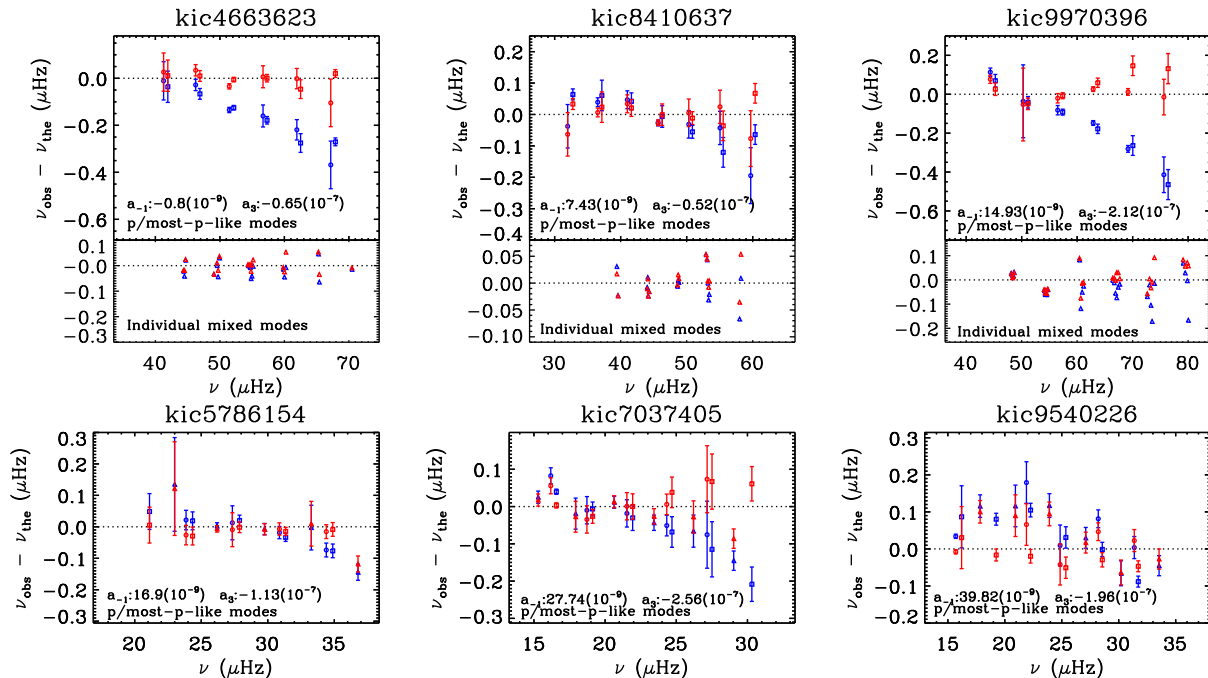
Figure 8. Frequency offsets caused by the surface term of the best-fitting models of our six red giants. Three stars with their $l = 1$ mixed modes identified are shown on the top, where the upper panels include p and the most p-like modes for $l = 0$ and 2, and the lower panels contain p–g mixed modes for $l = 1$. The other three stars with only p and the most p-like modes are shown at the bottom. Blue and red symbols represent the frequency offsets before and after the surface correction. Open squares, triangles, and circles indicate $l = 0$, 1, and 2 modes. Error bars are observation uncertainties.
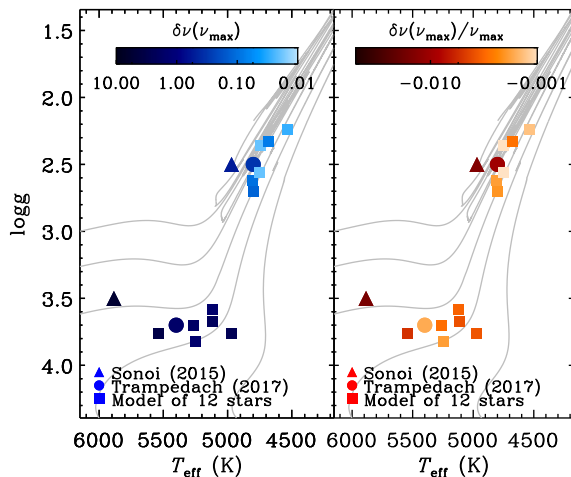
Figure 9. Absolute (left) and relative (right) frequency shifts across the HR diagram. The red giants studied in this work and six low-luminosity giants from Ball & Gizon (2017) are shown by squares. Filled triangles and circles are simulating predictions from Sonoi et al. (2015) and Trampedach et al. (2017). Frequency shifts are colour scaled according to the colour bar shown on the top.

6 CONCLUSIONS

The mixing-length parameter in stellar models, responsible for the strength of energy transport in convective regions, is important for the accuracy of the theoretical model. Moreover, the surface term affects the accuracy of asteroseismic modes and brings additional uncertainties in seismic products. In this work, six oscillating red giants in EBs were used to calibrate these parameters for evolved stars. Our main conclusions from the results are summarized as follows.
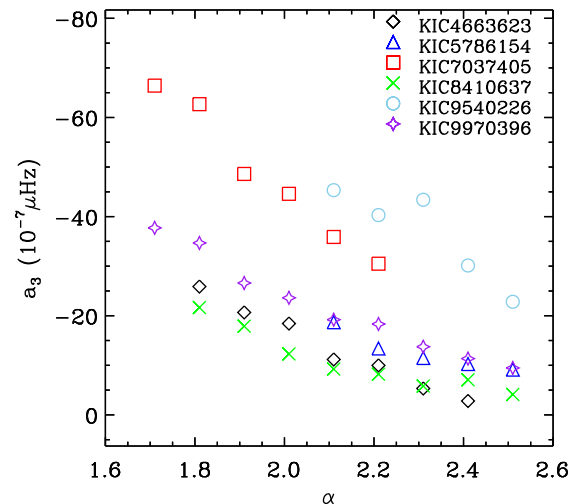

Figure 10. The correlation between the mixing-length parameter and the surface term. The coefficient of the cubic term (a_3) is from the best-fitting model for each star.

(i) The average mixing-length parameter of the six red giants is $\sim 1.14 \pm 0.07$ times the calibrated solar value, which is similar to the previous results based on the APOGEE sample (Tayar et al. 2017).

(ii) Our calibrated α is about 16 per cent higher than the value given by the 3D hydrodynamical simulations, possibly indicating that the 1D stellar model does not model the near-surface layers appropriately for the red giants with the input physics in this work.

(iii) The surface term was found to affect the mixed modes indirectly. Its effect on acoustic waves changes the frequency range where the p–g coupling happens.
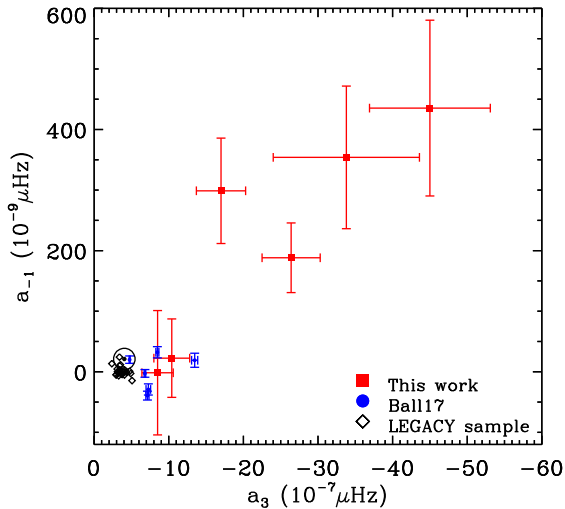
Figure 11. The correlation of two free coefficients (a_{-1} and a_3) in surface-correction expression (equation 6). Filled squares indicate the results of our red giants. Open circles represent the six low-luminosity giants from Ball & Gizon (2017). Open diamonds are 27 dwarfs from the LEGACY sample. Solar value is represented by $\odot$.

(iv) For our six red giants, established surface-correction methods fail to fix the surface effects in g-dominated modes, which cause a non-physical reordering in mixed modes.

(v) The surface term correlates with surface properties ($T_{\rm eff}$ and $\log g$) as well as the mixing-length parameter. The frequency offset decreases with stellar evolution on the red giant branch.

(vi) The two coefficients (a_{-1} and a_3) in the surface-correction expression (equation 6) significantly increase with stellar evolution due to the growth of mode inertia. They also show a linear correlation in the six red giants.

The calibrated results of the mixing-length parameter and the surface term on the six red giants can be additional references, along with the Sun, for further studies of red giants. The results can improve the accuracy of the theoretical models of stellar evolution and stellar oscillation by narrowing down the ranges of free parameters. High-precision measurements of the stellar atmosphere and other key parameters, such as the mass and radius, are required to further constrain theoretical models.
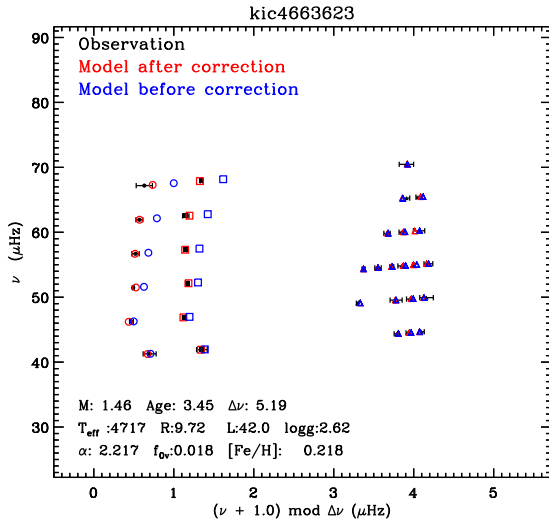
REFERENCES

Aerts C., Christensen-Dalsgaard J., Kurtz D. W., 2010, Asteroseismology. Springer, Berlin

Asplund M., Grevesse N., Sauval A. J., 2005, in Barnes T. G. III, Bash F. N., eds, ASP Conf. Ser. Vol. 336, Cosmic Abundances as Records of Stellar Evolution and Nucleosynthesis. Astron. Soc. Pac., San Francisco, p. 25

Asplund M., Grevesse N., Sauval A. J., Scott P., 2009, ARA&A, 47, 481

Ball W. H., Gizon L., 2014, A&A, 568A, 123

Ball W. H., Gizon L., 2017, A&A, 600, A128

Ball W. H., Beeck B., Cameron R. H., Gizon L., 2016, A&A, 592A, 159

Bedding T. R. et al., 2011, Nature, 471, 608

Bi S. L., Li T. D., Li L. H., Yang W. M., 2011, ApJ, 731, L42

Brogaard K. et al., 2017, MNRAS, submitted

Brown T. M., Gilliland R. L., Noyes R. W., Ramsey L. W., 1991, ApJ, 368, 599

Chaplin W. J., Elsworth Y., Isaak G. R., Marchenkov K. I., Miller B. A., New R., Pinter B., Appourchaux T., 2002, MNRAS, 336, 979

Christensen-Dalsgaard J., 2011, Astrophysics Source Code Library, record ascl:1109.002

Christensen-Dalsgaard J., Thompson M. J., 1997, MNRAS, 284, 527

Christensen-Dalsgaard J., Däppen W., Lebreton Y., 1988, Nature, 336, 634

Christensen-Dalsgaard J. et al., 1996, Science, 272, 1286

Christensen-Dalsgaard J., 2008, Ap&SS, 316, 113

Cox A. N. ed., 2000, in Allen's Astrophysical Quantities, 4th edn. Springer, New York, p. 341

Ferguson J. W., Alexander D. R., Allard F., Barman T., Bodnarik J. G., Hauschildt P. H., Heffner-Wong A., Tamanai A., 2005, ApJ, 623, 585

Frandsen S. et al., 2013, A&A, 556, A138

Gaulme P. et al., 2016, ApJ, 832, 121

Gough D. O., 1990, in Osaki Y., Shibahashi H., eds, Lecture Notes in Physics, Vol. 367, Progress of Seismology of the Sun and Stars. Springer-Verlag, Berlin, p. 283

Grevesse N., Sauval A. J., 1998, Space Sci. Rev., 85, 161

Huber D., Stello D., Bedding T. R., Chaplin W. J., Arentoft T., Quirion P.-O., Kjeldsen H., 2009, Commun. Asteroseismol., 160, 74

Jiang C. et al., 2011, ApJ, 742, 120

Kjeldsen H., Bedding T. R., Christensen-Dalsgaard J., 2008, ApJ, 683, L175

Lagarde N. et al., 2015, A&A, 580, A141

Lagarde N., Bossini D., Miglio A., Vrard M., Mosser B., 2016, MNRAS, 457, L59

Magic Z., Serenelli A., Weiss A., Chaboyer B., 2010, ApJ, 718, 1378

Magic Z., Weiss A., Asplund M., 2015, A&A, 573, A89

Mosser B. et al., 2014, A&A, 572, L5

Paxton B., Bildsten L., Dotter A., Herwig F., Lesaffre P., Timmes F., 2011, ApJS, 192, 3

Paxton B. et al., 2013, ApJS, 208, 4

Paxton B. et al., 2015, ApJS, 220, 15

Pérez Hernández F., García R. A., Corsaro E., Triana S. A., De Ridder J., 2016, A&A, 591, 99

Planck Collaboration XIII, 2016, A&A, 594, A13

Rogers F. J., Nayfonov A., 2002, ApJ, 576, 1064

Roxburgh I. W., Vorontsov S. V., 2003, A&A, 411, 215

Sonoi T., Samadi R., Belkacem K., Ludwig H.-G., Caffau E., Mosser B., 2015, A&A, 583, A112

Tayar J. et al., 2017, ApJ, 840, 17

Trampedach R., Stein R. F., 2011, ApJ, 731, 78

Trampedach R., Stein R. F., Christensen-Dalsgaard J., Nordlund Å, Asplund M., 2014, MNRAS, 445, 4366

Trampedach R., Aarslev M. J., Houdek G., Collet R, Christensen-Dalsgaard J., Stein R. F., Asplund M., 2017, MNRAS, 466, L43

APPENDIX A
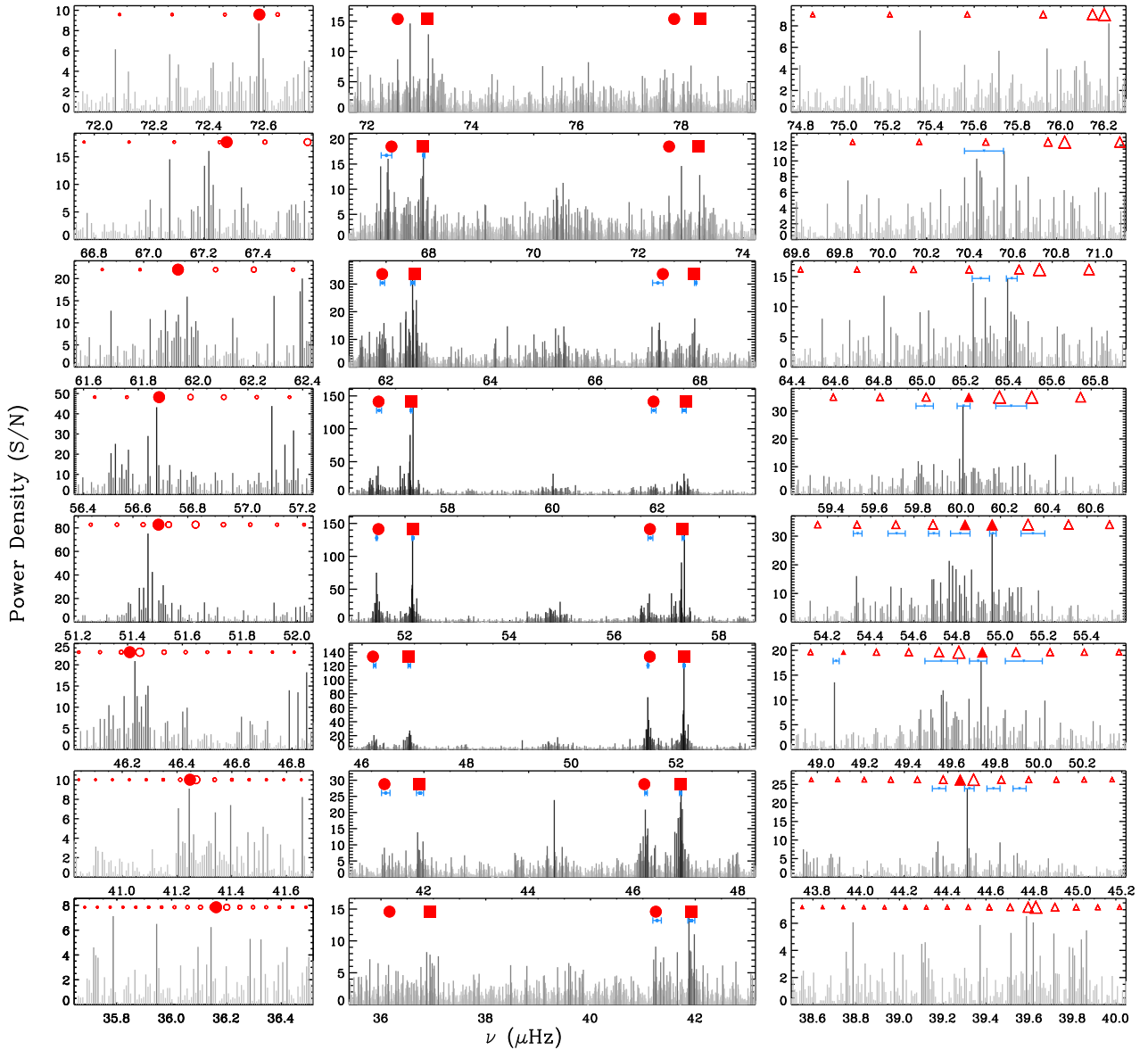
Figure A1. The peak-bagging process of individual mixed modes for KIC 4663623. The whole power spectrum is separated into eight radial-mode orders as shown in the middle. Close inspections of $l = 2$ and 1 modes are plotted on the left and right sides. The colour code was set as the same as that in Fig. 1, indicating the $\mathcal{P}_{signal}$ of each frequency bin. Red symbols plotted on the top are theoretical frequencies of the best-fitting model. Squares, circles, and triangles in the middle represent the p and most p-like modes for $l = 0$, 1, and 2. Filled symbols are the modes for picking the fitting models, and open symbols are those for guiding the identification of other mixed modes. Circles and triangles on the left and right indicate all theoretical mixed modes in each frequency bin. And their symbol size is scaled with $1/I^2$ (I is mode inertia) by reference to that of the most p-like mode in each degree and order. Larger size indicates the mode to be more p-like and less in inertia. Small blue symbols represent identified observed frequencies.

Figure A2. Observed and theoretical échelle diagram of KIC 4663623. Black symbols are observed modes. Blue and red symbols indicate model frequencies before and after the surface correction.
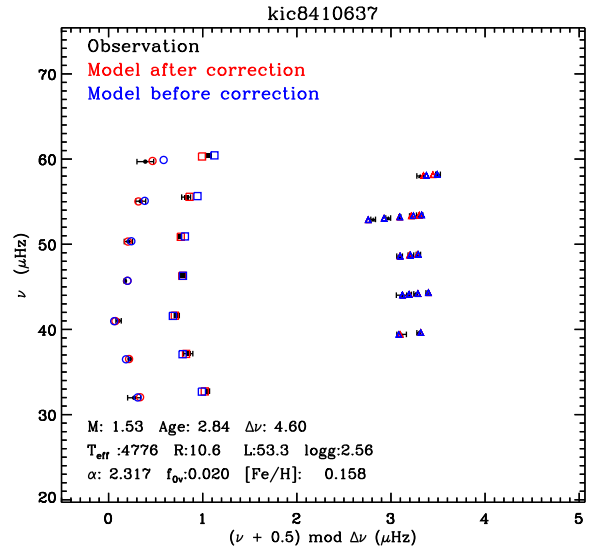
Figure A4. Same as Fig. A2, but for KIC 8410637.
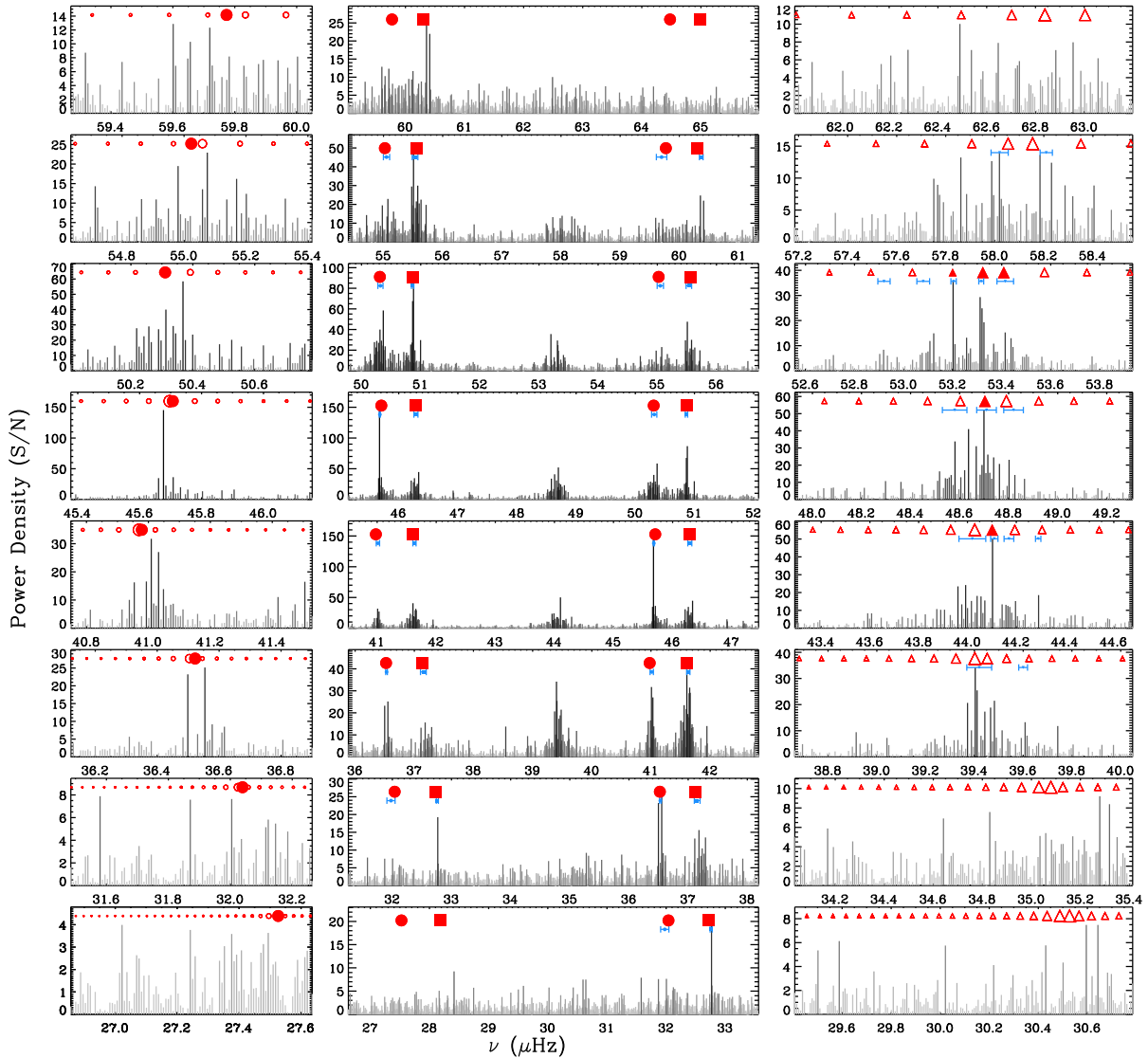
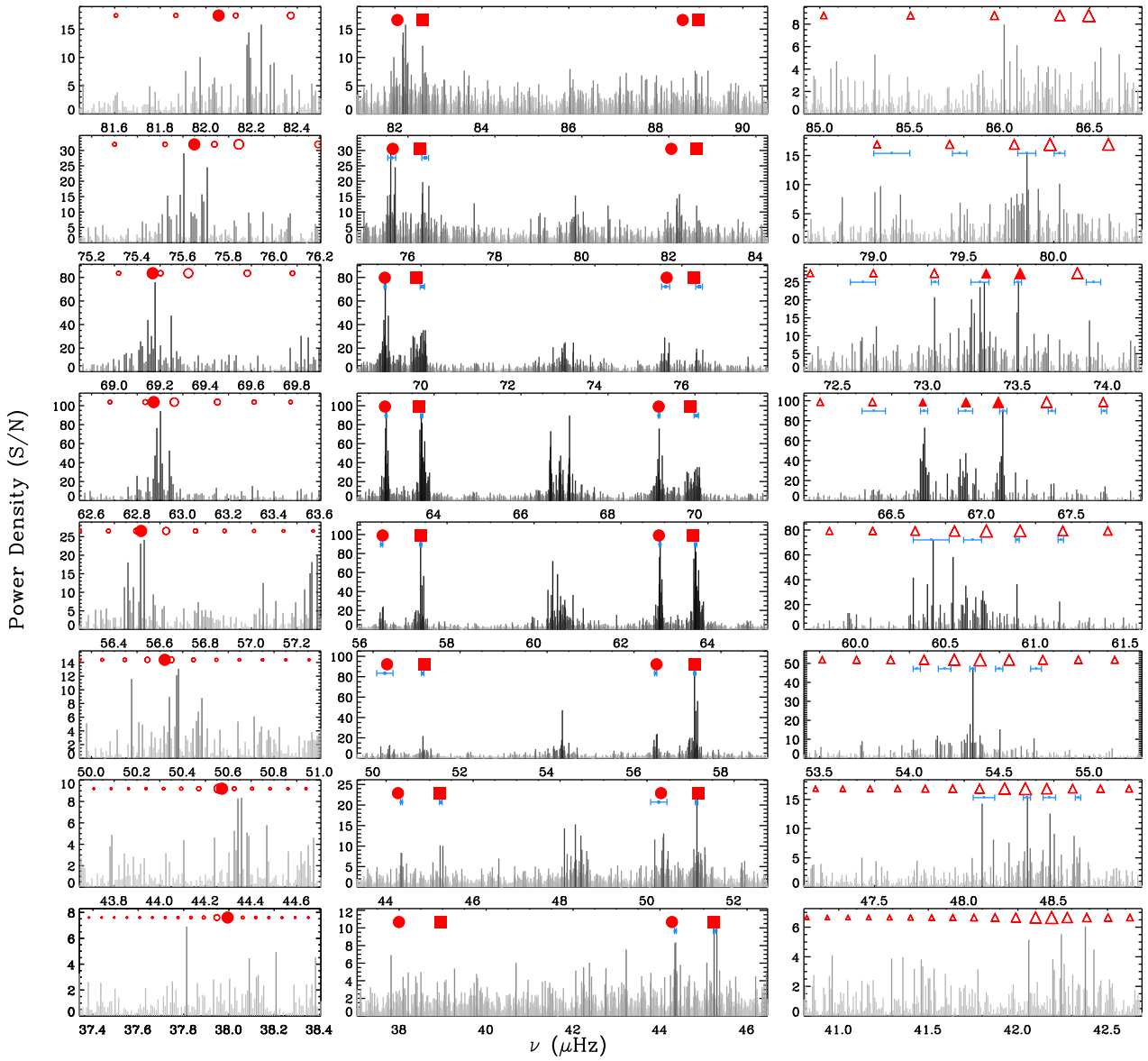**Figure A3.** Same as Fig. A1, but for KIC 8410637.

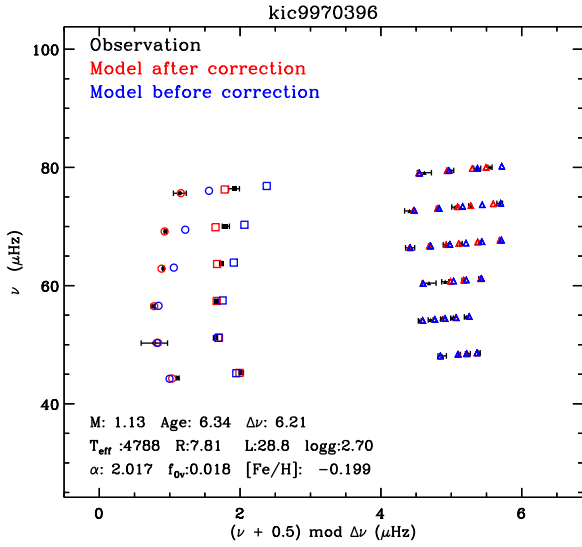**Figure A5.** Same as Fig. A1, but for KIC 9970396.
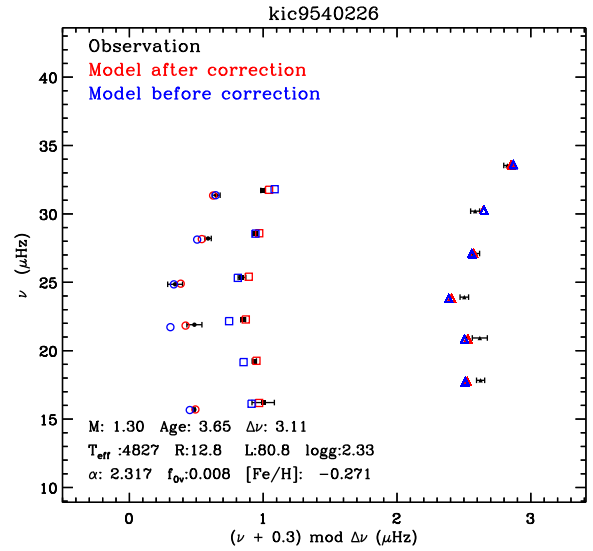
Figure A6. Same as Fig. A2, but for KIC 9970396.

Figure A7. Same as Fig. A2, but for KIC 5786154.
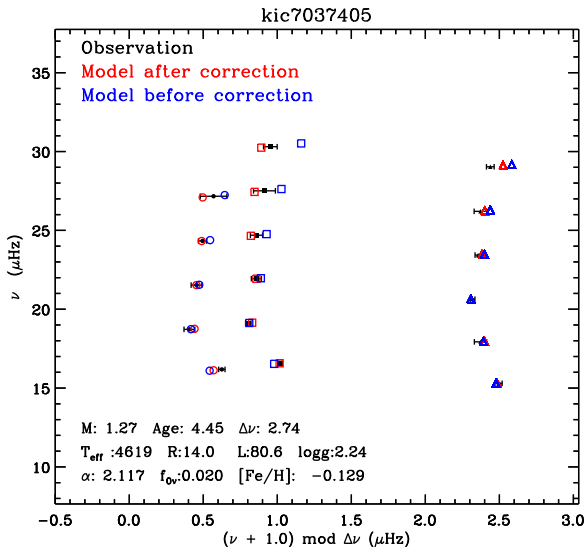
Figure A8. Same as Fig. A2, but for KIC 7037405.

Figure A9. Same as Fig. A2, but for KIC 9940226.

Table A1. Identified oscillation frequencies for star KIC 4663623.

l	ν (μHz)	σ (μHz)
	p and the most p-like modes	
2	41.271	0.081
0	41.924	0.066
2	46.240	0.024
0	46.900	0.022
2	51.458	0.011
0	52.144	0.009
2	56.684	0.046
0	57.305	0.015
2	61.929	0.043
0	62.509	0.039
2	67.187	0.101
0	67.903	0.016
0	72.820	0.298
	Individual mixed modes	
1	44.360	0.031
1	44.499	0.022
1	44.610	0.030
1	44.732	0.028
1	49.067	0.014
1	49.550	0.075
1	49.720	0.041
1	49.930	0.085
1	54.340	0.022
1	54.520	0.041
1	54.692	0.025
1	54.814	0.045
1	54.965	0.015
1	55.150	0.055
1	59.830	0.043
1	60.010	0.028
1	60.230	0.071
1	65.270	0.042
1	65.413	0.025
1	70.465	0.090

Table A2. Identified oscillation frequencies for star KIC 8410637.

l	ν (μHz)	σ (μHz)
	p and the most p-like modes	
2	41.013	0.028
0	41.632	0.027
2	45.682	0.009
0	46.291	0.034
2	50.319	0.043
0	50.864	0.020
2	55.051	0.052
0	55.533	0.047
2	59.701	0.088
0	60.371	0.031
	Individual mixed modes	
1	39.420	0.051
1	39.600	0.018
1	44.020	0.055
1	44.110	0.015
1	44.170	0.02
1	44.290	0.011
1	48.583	0.048
1	48.712	0.043
1	48.818	0.039
1	52.920	0.025
1	53.080	0.026
1	53.203	0.011
1	53.316	0.010
1	53.414	0.034
1	58.020	0.035
1	58.210	0.025

Table A3. Identified oscillation frequencies for star KIC 9970396.

l	ν (μHz)	σ (μHz)
	p and the most p-like modes	
2	44.351	0.021
0	45.255	0.032
2	50.270	0.187
0	51.138	0.029
2	56.496	0.023
0	57.396	0.015
2	62.895	0.012
0	63.717	0.023
2	69.173	0.017
0	70.031	0.050
2	75.626	0.091
0	76.395	0.077
	Individual mixed modes	
1	48.110	0.060
1	48.350	0.020
1	48.475	0.034
1	48.635	0.016
1	54.040	0.018
1	54.195	0.034
1	54.350	0.045
1	54.498	0.020
1	60.375	0.055
1	60.672	0.070
1	60.899	0.012
1	60.899	0.011
1	61.140	0.015
1	66.400	0.065
1	66.680	0.020

Table A3 –*continued*

l	ν (μHz)	σ (μHz)
1	66.910	0.041
1	67.120	0.018
1	67.390	0.023
1	67.680	0.015
1	72.640	0.070
1	73.040	0.022
1	73.290	0.051
1	73.501	0.019
1	73.921	0.041
1	79.080	0.080
1	79.477	0.040
1	79.800	0.063
1	80.050	0.018

Table A4. Identified oscillation frequencies for star KIC 5786154.

l	ν (μHz)	σ (μHz)
	p and the most p-like modes	
0	21.112	0.056
1	22.647	0.048
2	23.858	0.030
0	24.347	0.028
1	26.187	0.010
2	27.340	0.054
0	27.874	0.016
1	29.758	0.017
2	30.876	0.019
0	31.343	0.012
1	33.271	0.071
2	34.396	0.021
0	34.882	0.021
1	36.781	0.025

Table A5. Identified oscillation frequencies for star KIC 7037405.

l	ν (μHz)	σ (μHz)
	p and the most p-like modes	
1	15.310	0.016
2	16.182	0.021
0	16.575	0.007
1	17.929	0.041
2	18.723	0.036
0	19.120	0.018
1	20.635	0.016
2	21.530	0.036
0	21.935	0.034
1	23.432	0.020
2	24.331	0.027
0	24.695	0.041
1	26.208	0.043
2	27.164	0.089
0	27.508	0.074
1	29.034	0.025
0	30.307	0.046

Table A6. Identified oscillation frequencies for star KIC 9540226.

l	ν (μHz)	σ (μHz)
p and the most p-like modes		
2	15.694	0.005
0	16.208	0.083
1	17.833	0.030
0	19.244	0.016
1	20.929	0.056
2	21.898	0.056
0	22.262	0.018
3	22.819	0.016
1	23.915	0.032
2	24.785	0.030
0	25.355	0.028
1	27.103	0.028
2	28.203	0.024
0	28.556	0.019
1	30.199	0.033
2	31.366	0.029
0	31.714	0.014
1	33.542	0.027

This paper has been typeset from a TEX/LATEX file prepared by the author.